Journal of Crystal Growth 498 (2018) 10–16

Contents lists available at ScienceDirect

Journal of Crystal Growth

journal homepage: www.elsevier.com/locate/jcrysgro

Formation of modulated structures induced by oxygen vacancies in α-Fe_2O_3 nanowires

Tao Li[a,1], Honglei Feng[a,1], Yiqian Wang[a,*], Chao Wang[a], Wenhui Zhu[b], Lu Yuan[b], Guangwen Zhou[b]

[a] College of Physics, Qingdao University, No. 308 Ningxia Road, Qingdao 266071, PR China
[b] Department of Mechanical Engineering & Multidisciplinary Program in Materials Science and Engineering, State University of New York, Binghamton, NY 13902, USA

ARTICLE INFO

Communicated by K. Deppert

Keywords:
A1. Microsturcture
A1. Modulated structure
A1. Oxygen vacancy
B1. α-Fe_2O_3 nanowires

ABSTRACT

Two modulated structures caused by long-range ordering of oxygen vacancies have been observed in α-Fe_2O_3 nanowires (NWs) produced after oxidation of Fe, one being ten times $(3\,0\,\bar{3}\,0)$ interplanar spacing and the other being six times $(1\,1\,\bar{2}\,0)$ interplanar spacing. Both types of oxygen vacancy ordering structures have a similar modulation periodicity of 1.45 or 1.50 nm with corresponding atomic ratios of Fe and O (Fe/O) of 0.7407 and 0.7273, respectively. The Fe/O ratios in the NWs with oxygen-vacancy ordering are very close to that of Fe_3O_4 (0.7500). The similar Fe/O ratio between NWs and Fe_3O_4 may explain the similar modulation periodicity of different oxygen-vacancy orderings. Electron energy-loss spectroscopy studies show that the Fe/O ratio of NWs is close to that of Fe_3O_4 when oxygen atoms are not sufficient, which makes the NWs energetically favorable. The elucidation of the mechanism governing the formation of the modulated structures in α-Fe_2O_3 NWs is critical for controlling the microstructure and correspondingly physicochemical properties of NWs.

1. Introduction

Nanowires (NWs) are one-dimensional nanomaterials with a large aspect ratio (length/diameter) and show unique properties that are tunable by varying the aspect ratio. A wide variety of nanowires have been synthesized and are used in many fields. For example, flexible electrochromic supercapacitor hybrid electrodes based on tungsten oxide films and silver nanowires demonstrate excellent electrochemical performance [1]. TiO_2 nanowires as a photocatalyst manifest good photocatalytic activity for degradation of rhodamine B [2]. One-dimensional hematite (α-Fe_2O_3) nanomaterials are a promising alternative for applications in catalysis [3], water splitting [4], sensors [5], dye-sensitized solar cells [6], and supercapacitor [7]. Until now, α-Fe_2O_3 NWs have been successfully synthesized by various methods such as templates [8], hydrothermal methods [9], sol-gel-mediated reactions [10], solvothermal methods [11], gas decomposition [12], direct thermal oxidation [13], chemical vapor deposition (CVD) [14], and plasma-enhanced chemical vapor deposition (PECVD) [15]. Point defects such as oxygen vacancies are often found in the α-Fe_2O_3 NWs synthesized by the above methods. Particularly, modulated structures produced by long-range ordering of oxygen vacancies are found in the α-Fe_2O_3 NWs with ten times $(3\,0\,\bar{3}\,0)$ interplanar spacing [16–20]. In addition, oxygen-vacancy orderings with a periodicity of four times $(1\,\bar{1}\,0\,2)$ interplanar spacing are also observed in the α-Fe_2O_3 NWs [19,20]. More interestingly, the oxygen-vacancy ordering in α-Fe_2O_3 could result in *p*-type conductivity and plays an important role in *n-p* transition [16], indicating that the electronic properties of oxygen-deficient α-Fe_2O_3 NWs could be associated with the type of oxygen-vacancy ordering in the NWs. However, the origin of such oxygen-vacancies ordering in the NWs still remains unclear.

Here, α-Fe_2O_3 NWs were produced on a large scale through thermal oxidation of iron foils [21]. In our previous studies [22], stacking faults have been found in the synthesized NWs. In this work, we show the formation of two superstructures in the α-Fe_2O_3 NWs, which involve the long-range ordering of oxygen vacancies on every tenth $(3\,0\,\bar{3}\,0)$ plane with a periodicity of 1.45 nm and the ordering of oxygen vacancies six times $(1\,1\,\bar{2}\,0)$ interplanar spacing with a periodicity of 1.50 nm. By determining the atomic ratios of Fe and O (Fe/O) of two different modulated structures, we find that their ordering distances of 1.45 and 1.50 nm are very close to the favorable ratio (0.7500) for Fe_3O_4. By extensive high-resolution transmission electron microscopy (HRTEM) observations, electron energy-loss spectroscopy (EELS) measurements and HRTEM simulations, we demonstrate that the Fe/O ratio in the oxygen-deficient α-Fe_2O_3 NWs is close to that of Fe_3O_4, which

* Corresponding author.
E-mail address: yqwang@qdu.edu.cn (Y. Wang).
[1] These authors contributed equally to this work.

https://doi.org/10.1016/j.jcrysgro.2018.05.031
Received 1 February 2018; Received in revised form 26 May 2018; Accepted 28 May 2018
Available online 29 May 2018
0022-0248/

makes the NWs energetically favorable.

2. Experimental

The Fe_2O_3 NWs were synthesized by the thermal oxidation of Fe foils. First, the high-purity (99.99%) Fe foils were rinsed with deionized water followed by ultrasonication in acetone for 5 min. Then the cleaned Fe substrates were put on a substrate heater in a vacuum chamber, and the temperature was monitored using a K-type thermocouple in contact with the heater. The chamber was pumped to a vacuum of about 2×10^{-6} Torr, and then filled with 200 Torr of oxygen gas (oxygen purity: 99.999%) (1 Torr = 1.33322×10^2 Pa). Subsequently, the chamber was sealed and the Fe foil was heated to 600 °C at a rate of 20 °C/min in the oxygen gas. After the Fe foil was oxidized for 1 h, it was then cooled down in the same oxygen atmosphere to room temperature at a rate of ~10 °C/min.

The surface morphologies of oxidized samples were examined using FEI Supra 55VP field-emission scanning electron microscope (SEM). The crystal structure of the sample was analyzed by SmartLab XRD with Cu-Kα_1 radiation (λ = 1.5406 Å). Transmission electron microscope (TEM) samples of Fe_2O_3 NWs were prepared by peeling off the black product from the oxidized surface of the Fe foils, ultrasonicating them in ethanol for several minutes, and dispersing a drop onto a holy-carbon-film-coated copper grid. Selected-area electron diffraction (SAED), bright field (BF), and HRTEM examinations were carried out using a JEOL JEM 2100F TEM operating at 200 kV. EELS was performed on an FEI Tecnai F20 TEM. The EELS spectra were acquired in an image mode with a collection half angle of ~16 mrad.

3. Results and discussion

Fig. 1(a) shows a cross-sectional SEM image of α-Fe_2O_3 NWs. It can be seen that the oxidized Fe foil is covered by a high density of NWs with a diameter varying from 50 to 150 nm and a length up to ~6 μm. Fig. 1(b) displays the XRD pattern of the oxidized Fe substrate. All the diffraction peaks can be indexed to rhombohedral structure of α-Fe_2O_3 (JCPDS no.: 01-1053). No notable peak of impurities can be detected, which indicates that no other phase formed in the top section of the oxidized surface.

The microstructures of as-synthesized α-Fe_2O_3 NWs were extensively examined by TEM. An oxygen-vacancy superstructure was observed in α-Fe_2O_3 NWs with a modulation periodicity of ten times $(3\,0\,\bar{3}\,0)$ interplanar spacing. Fig. 2(a) shows a typical low-magnification BF TEM image of single α-Fe_2O_3 nanowire (NW). Fig. 2(b) shows a typical HRTEM image obtained from region b of the NW marked in Fig. 2(a), in which blurred ordering bands are visible and parallel to the axial direction of the NW. The sequential periodic structure with a regular spacing of 1.45 nm marked by white arrows can be observed in Fig. 2(b). To show the superstructure more clearly, an enlarged HRTEM image is shown in Fig. 2(c), from which the distance of the ordering bands is found to be ten times the spacing of $(3\,0\,\bar{3}\,0)$ plane. Fig. 2(d) is a typical SAED pattern of the α-Fe_2O_3 NW in Fig. 2(a). There are 9 superlattice diffraction spots marked by red arrows in Fig. 2(d) (one spot was covered by strong transmission and diffraction spots) between the two diffraction spots, indicating the oxygen-vacancy ordering is ten times the spacing of $(3\,0\,\bar{3}\,0)$ planes. Our results are similar to the previous reports [16–20].

To confirm the structure of this oxygen-vacancy ordering, we constructed a superstructural model, $a' = b' = 10a = 10b = 5.034$ nm and $c' = c = 1.375$ nm [as shown in Fig. 3(a)], with oxygen vacancies on every tenth $(3\,0\,\bar{3}\,0)$ plane, where the blue balls, red balls and white balls represent the iron cations, oxygen anions and oxygen vacancies, respectively. It is noticeable that the ordering feature coincides with the column of oxygen vacancies in the $(3\,0\,\bar{3}\,0)$ plane, wherein the oxygen vacancies form in pairs and aggregate linearly. The HRTEM image simulation was carried out using xHREM software. The simulated $[0\,0\,0\,1]$ zone-axis HRTEM image [inset of Fig. 3(b)] was obtained using a defocus of 40 nm, a thickness of 55 nm. It matches well with the experimental image shown in Fig. 3(b). The SAED pattern in Fig. 2(d) is same as the fast Fourier transform (FFT) image in Fig. 3(d), where extra maxima are indicated by red arrows and the main diffraction spots are marked by yellow circles. Based on the above analyses, we conclude that the oxygen-vacancy ordering is formed in the α-Fe_2O_3 NWs on every tenth $(3\,0\,\bar{3}\,0)$ plane with an ordering distance of 1.45 nm.

In addition to the ordering on every tenth $(3\,0\,\bar{3}\,0)$ plane, another superstructure on every sixth $(1\,1\,\bar{2}\,0)$ plane was shown in Fig. 4. Fig. 4(a) shows a BF TEM image of as-synthesized single α-Fe_2O_3 NW. Fig. 4(b) is a typical HRTEM image obtained from area b shown in Fig. 4(a), which shows visible bands separated by a distance of 1.5 nm which is six times the spacing of $(1\,1\,\bar{2}\,0)$ plane, as shown by white arrows. The enlarged HRTEM image is presented in Fig. 4(c) for detailed examination of the HRTEM image. In the SAED pattern [Fig. 4(d)], there are 5 extra spots between the transmission spot and $(1\,1\,\bar{2}\,0)$ diffraction spot (3 spots was covered by strong transmission spots) with a periodicity six times $(1\,1\,\bar{2}\,0)$ interplanar spacing that highlights the ordering feature.

Similarly, we constructed a superstructure model with oxygen vacancies in every sixth plane of $(1\,1\,\bar{2}\,0)$ [Fig. 5(a)] with lattice parameters as follows: $a' = b' = 10a = 10b = 5.034$ nm and $c' = c = 1.375$ nm. The corresponding HRTEM image was simulated using a defocus of 35 nm and a thickness of 55 nm. The $[0\,0\,0\,1]$ zone-axis simulated HRTEM image [the inset in Fig. 5(b)] matches well with the experimental image [Fig. 5(b)]. Fig. 5(c) is a FFT pattern of the simulated HRTEM image, which matches with the SEAD pattern shown in Fig. 4(d) and confirms the existence of six times $(1\,1\,\bar{2}\,0)$ oxygen-vacancy ordering.

The formation of oxygen-vacancy ordering in α-Fe_2O_3 NW is still unclear, although many kinds of oxygen-vacancy ordering have been reported, *i.e.*, ten times $(3\,0\,\bar{3}\,0)$ interplanar spacing with a distance of 1.45 nm [16–20], four times $(1\,\bar{1}\,0\,2)$ interplanar spacing with a distance of 1.47 nm [19,20]. Chen et al. [19] revealed that the formation of oxygen-vacancy pairs at the nearest-neighbor sites is energetically favorable. When pairs of oxygen vacancies form in a chain, all of the iron and oxygen ions next to the oxygen vacancies have the same state, presumably considered as lower internal energy. However, why do the different types of oxygen-vacancy ordering lead to an equivalent ordering distance? They believed that the lattice mismatch induced strain between the substrate and NWs at the growth temperatures is the main reason for oxygen-vacancy ordering [19]. But the theory of lattice mismatch cannot explain the oxygen-vacancy ordering presented in our experiment.

First, the nanowires and nanobelts in the experiment of Chen et al. are directly grown from the bulk iron alloy. However, in our experiment, the oxidation at 600 °C results in the formation of three oxide layers with a much thicker (~5 μm) FeO layer that lies directly above the Fe substrate, an intermediate Fe_3O_4 layer (~2 μm), and a thin outer Fe_2O_3 layer (~400 nm) on which Fe_2O_3 NWs are formed [23]. In this way, oxygen-vacancy ordering does not come from the lattice mismatch induced strain between the substrate (Fe_2O_3 layer) and the Fe_2O_3 NWs. Second, it is believed that stress exists in different iron oxide layers. However, sample estimations of the density of different oxide layers show that the volume increase in the FeO layer is 77% with respect to Fe, the volume of Fe_3O_4 shows a 255% increase with respect to FeO, while the formation of Fe_2O_3 is accompanied by a 32% decrease in the molecular volume [24]. Since the three different iron oxide layers have large thickness, the stresses generated at the interfaces of layers can be released by a number mechanisms including cracking and spalling of the oxide scales and plastic deformation of the oxide layers instead of oxygen-vacancy ordering [23]. This means that the stress should be mainly accumulated in the Fe_3O_4 and FeO layers and can be released by cracking. Thus, the stress cannot directly affect the oxygen-vacancy ordering observed in the α-Fe_2O_3 NWs.

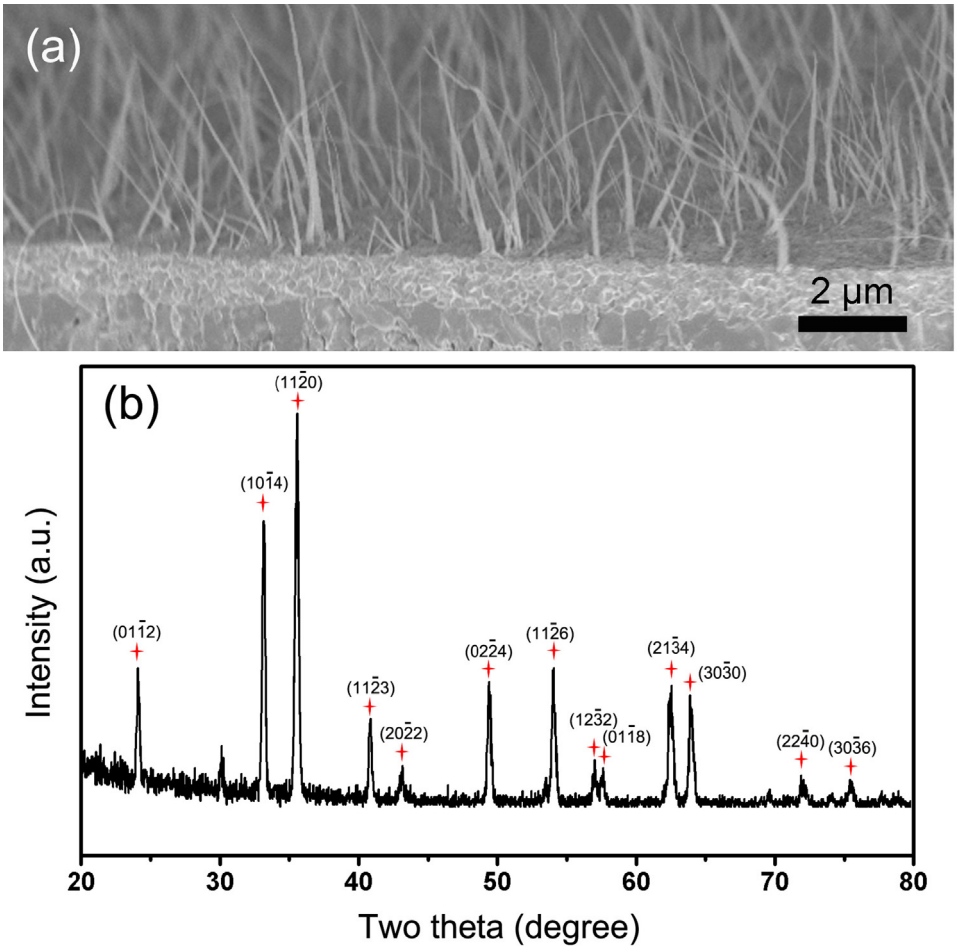

Fig. 1. (a) Cross-sectional SEM image of α-Fe_2O_3 NWs; (b) XRD pattern from the oxidized Fe foil.

Considering Fe and O ratio in α-Fe_2O_3 NWs with oxygen-vacancy planes, a hard-ball model, with oxygen atoms removed along different oxygen planes is shown in Fig. 6, where the red balls, blue balls and white balls represent the oxygen anions, iron cations, and oxygen vacancies caused by oxygen deficiency, respectively. In the pure α-Fe_2O_3 NW, we assume that there are 2n Fe atoms and 3n O atoms (n represents positive integers). In this way, $Fe_{2n}O_{3n}$ constitutes the whole pure α-Fe_2O_3 NW and the atomic ratios of Fe and O (Fe/O) is 2n/3n = 0.6667. Fig. 6(a) shows a hard ball model, with oxygen atoms removed along the ten periodic distance of (3 0 $\bar{3}$ 0) interplanar spacing so the NW consists of 2n Fe atoms and (3n-3n/10) O atoms and ratio of Fe/O is $\frac{2n}{3n-3n/10} = 0.7407$. α-$Fe_2O_3$ NWs with the oxygen-vacancy ordering along four times the distance of (1 $\bar{1}$ 0 2) interplanar spacing consist of 2n Fe atoms and (3n-3n/12) O atoms and the Fe/O ratio is $\frac{2n}{3n-3n/12} = 0.7273$ shown in Fig. 6(b). Fig. 6(c) shows a superstructure model with oxygen vacancies in every sixth plane of (1 1 $\bar{2}$ 0), and the Fe/O ratio is $\frac{2n}{3n-3n/12} = 0.7273$ which is identical to the value of the four times the distance of (1 $\bar{1}$ 0 2) interplanar spacing. Interestingly, the Fe/O ratio in Fe_3O_4 is 0.7500, which is very close to the value of 0.7407 or 0.7273 for the oxygen vacancy ordered superstructures described above.

It is no coincidence that the Fe/O ratio of the α-Fe_2O_3 NWs with the oxygen-vacancy planes described above is similar to that of Fe_3O_4. We believe that it is the main reason for formation of different ordered structures with the similar vacancy-ordering distances. According to the tip growth mechanism of NWs, during the growth of the α-Fe_2O_3 NWs, Fe atoms diffuse fast along the NWs from the bottom to the tip [21,25]. However, the diffusion of O atoms along the nanowire can be generally neglected compared with Fe atoms [20]. Then oxygen-vacancy orderings are created in α-Fe_2O_3 NWs due to the increased mobility of iron atoms and the unavailable oxygen atoms to form pure α-Fe_2O_3 NWs. The α-Fe_2O_3 NWs can be theoretically grown until oxygen atoms are supplied to the surface. Moreover, it is demonstrated that Fe_3O_4 is the more stable than Fe_2O_3 when oxygen atoms are unavailable [21,26]. Thus, the stoichiometric ratio of Fe and O atom can be close to 0.7500 which is a favorable ratio for Fe_3O_4 if the supply of oxygen atoms is not sufficiently fast.

To study the chemical compositions of α-Fe_2O_3 NWs, EELS was carried out. To compare with α-Fe_2O_3 NWs, α-Fe_2O_3 powder was chosen as a counterpart to investigate the differences in fine structures of O *K*-edges and Fe-$L_{2,3}$ edges. Fig. 7 shows the EELS spectra of O *K*-edges and Fe-$L_{2,3}$ edges for the α-Fe_2O_3 powder and single α-Fe_2O_3 NW with oxygen-vacancy orderings. In Fig. 7(a), four peaks, labeled a-d, can be found in the oxygen *K*-edge energy-loss near-edge fine structure (ELNES). It can be clearly seen from Fig. 7(a) that the intensities of both peak a and peak b decrease evidently. It was previously demonstrated that the decreased intensities in peaks a and b of EELS spectra for α-Fe_2O_3 nanostructures are associated with the oxygen vacancies inside the nanostructures [14,27]. Thus, the lower the peak intensities in EELS spectra, the higher content of the oxygen vacancies in α-Fe_2O_3. The corresponding Fe $L_{2,3}$ edges spectra for α-Fe_2O_3 powder, and single α-Fe_2O_3 NW are shown in Fig. 7(b). It can be seen that the Fe-$L_{2,3}$ edges are characterized by two white-line peaks close to the ionization threshold. The energy separation of two peaks reflects the spin-orbit splitting of the initial states in the transitions from $2p^{3/2}$ to $3d^{3/2}$, $3d^{5/2}$ and from $2p^{1/2}$ to $3d^{3/2}$. The relative intensity of two peaks depends on the number of electrons in the final (3*d*) state, and therefore varies with oxidation state. Therefore the Fe-*L* white-line measurements can

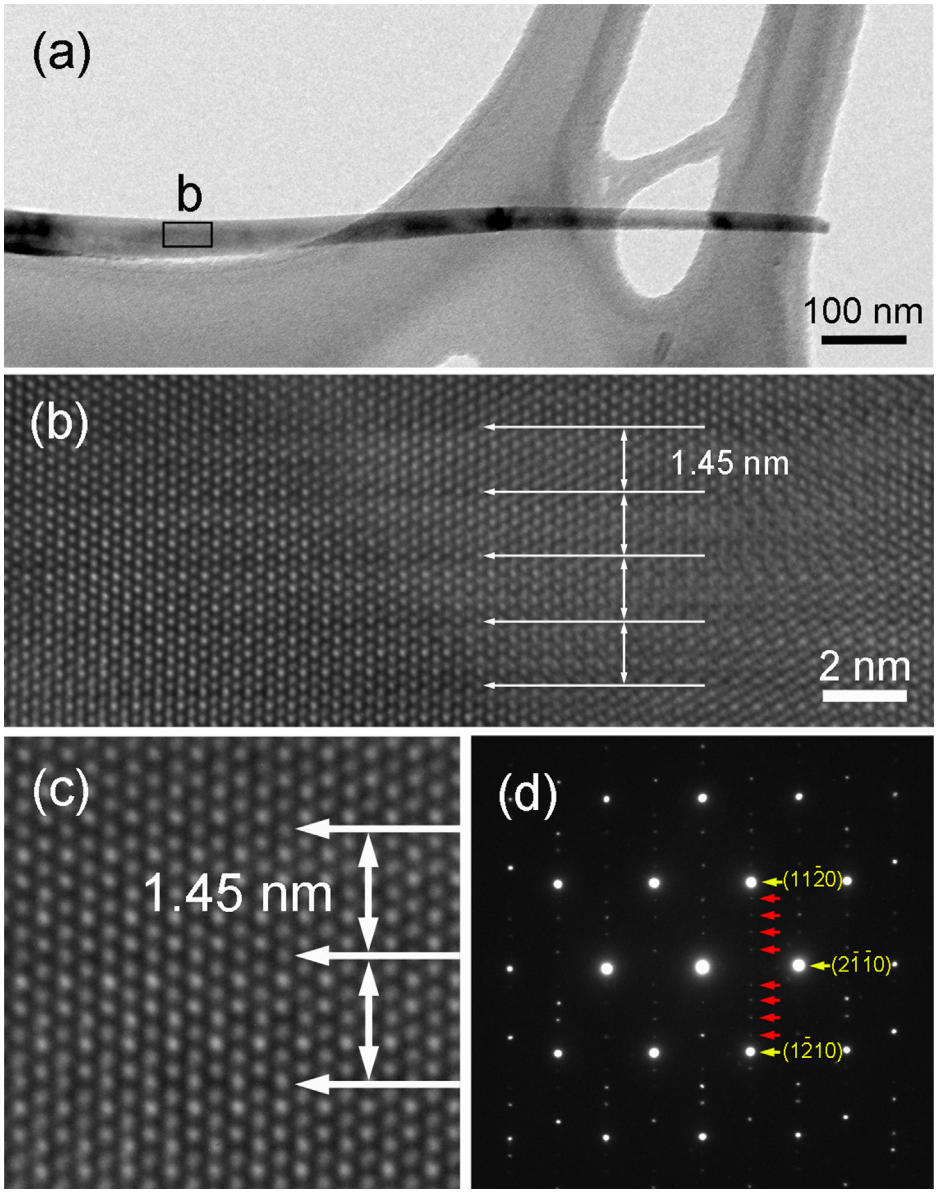

Fig. 2. (a) Typical BF TEM image of α-Fe_2O_3 NW with oxygen-vacancy ordering; (b) Typical HRTEM image from region b in (a); (c) An enlarge HRTEM image; (d) SAED pattern from region b in (a).

provide us with information about oxidation state (or ionization status) of Fe by determining the relative intensity and position of individual L_3 and L_2 edges, respectively [28]. Quantification of the EELS spectra in Fig. 7(b) shows that the separation between the L_2 and L_3 lines remains constant (~12.6 eV) for the α-Fe_2O_3 powder, but chemical shifts of L_3 line about 0.4 eV for the NW are detected. It was reported that the position of the L_3 line is sensitive to the valence states of the transition metal oxide [27]. Therefore, the chemical shifts for the L_3 line confirm a

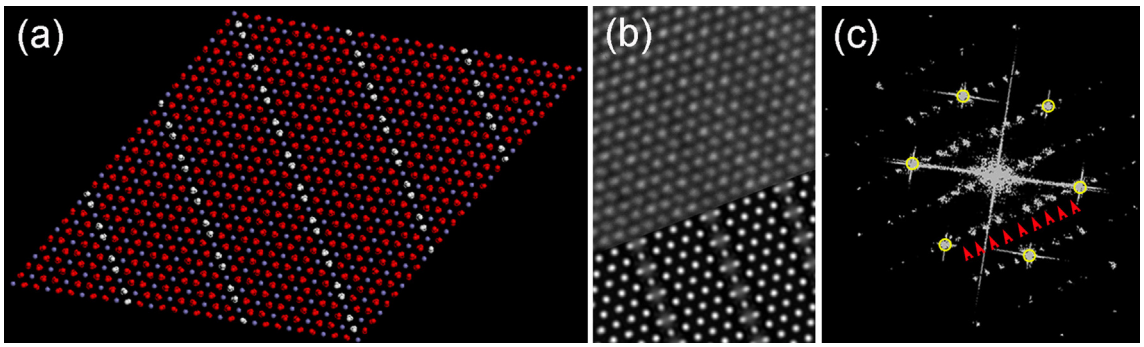

Fig. 3. (a) Superstructure model constructed with $a' = 10a_{\alpha\text{-}Fe2O3}$, $b' = 10b_{\alpha\text{-}Fe2O3}$, $c' = c_{\alpha\text{-}Fe2O3}$, and oxygen-vacancy ordering ten times $(3\,0\,\bar{3}\,0)$ interplanar spacing; (b) Typical HRTEM image of α-Fe_2O_3 NW with oxygen-vacancy ordering. The inset in (b) is the simulated HRTEM image; (c) FFT of the HRTEM image.

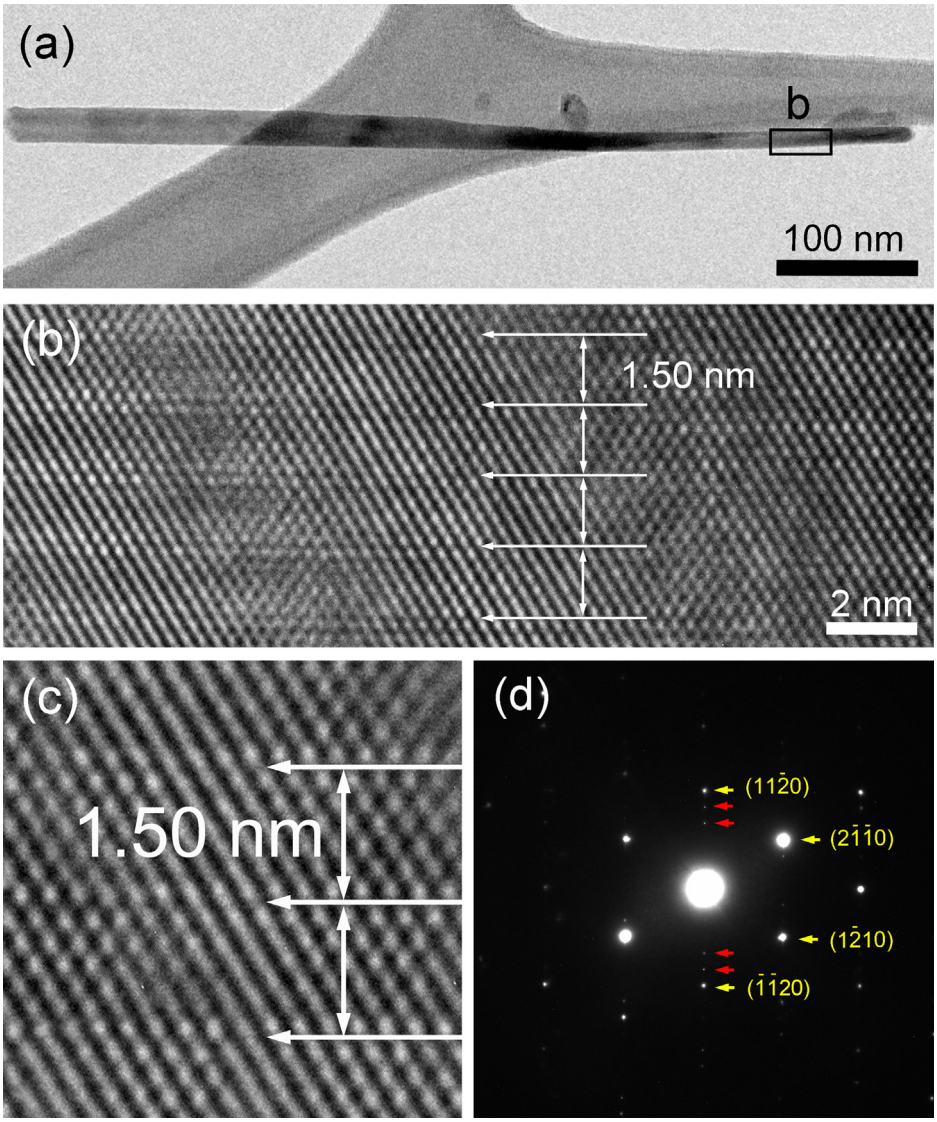

Fig. 4. (a) Typical BF TEM image of an α-Fe_2O_3 NW; (b) Typical HRTEM image of the α-Fe_2O_3 NW from region b in (a); (c) Enlarged HRTEM image; (d) SAED pattern from region A in (a).

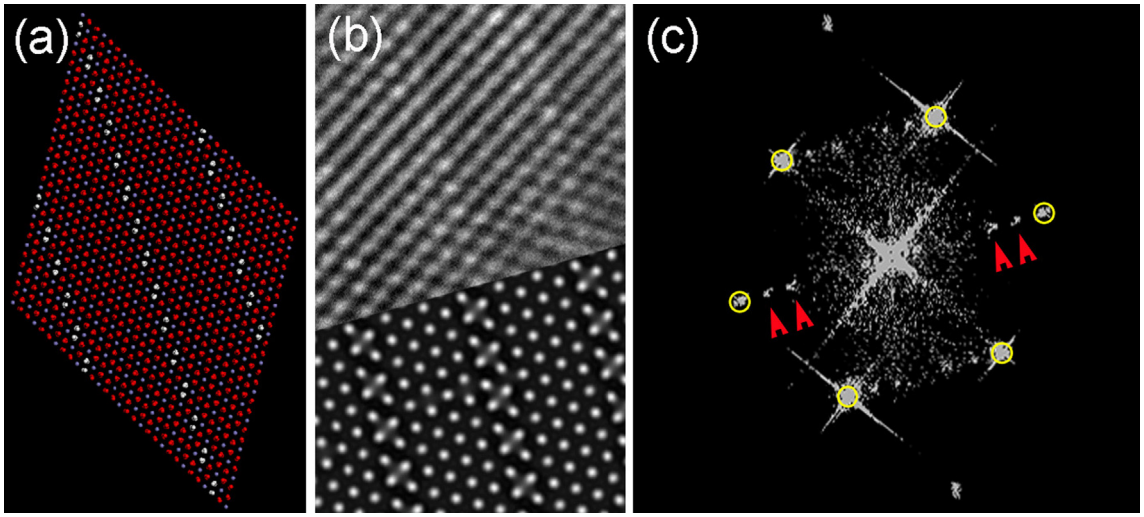

Fig. 5. (a) superstructure model constructed with $a' = 10a_{\alpha\text{-}Fe2O3}$, $b' = 10b_{\alpha\text{-}Fe2O3}$, $c' = c_{\alpha\text{-}Fe2O3}$, and the oxygen-vacancy ordering six times $(1\,1\,\bar{2}\,0)$ interplanar spacing; (b) Typical HRTEM image of α-Fe_2O_3 NW with oxygen-vacancy ordering. The inset in (b) is the simulated HREM image; (c) FFT image of the HRTEM image.

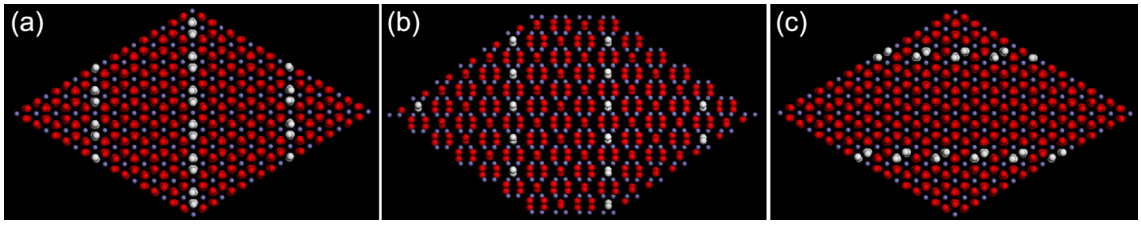

Fig. 6. Schematic drawing of three different oxygen-vacancy orderings with a periodicity of ten times $(30\bar{3}0)$ (a), four times $(1\bar{1}02)$ (b) and six times $(11\bar{2}0)$ (c) interplanar spacing.

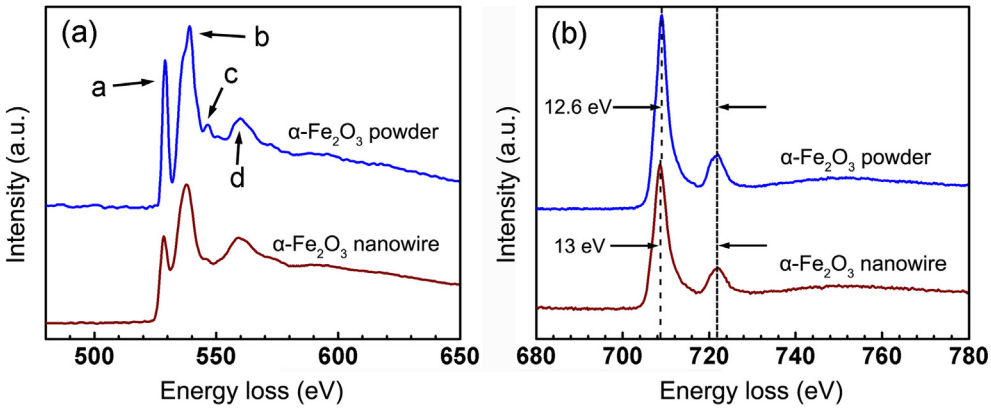

Fig. 7. (a) Typical O *K*-edge ELNES spectra for the pure α-Fe_2O_3 NWs and α-Fe_2O_3 NWs with oxygen-vacancy ordering; (b) The corresponding EELS spectra of $L_{2,3}$ edge for the pure α-Fe_2O_3 NWs and α-Fe_2O_3 NWs with oxygen-vacancy ordering.

change in the partial oxidation states from Fe^{3+} to Fe^{2+}, which is consistent with other reports [27]. Then it is concluded that more oxygen vacancies exist in the NW. Quantification of the EELS spectra shows that the atomic ratios of Fe and O are 0.6667 ± 0.03 for the α-Fe_2O_3 powder, and 0.7143 ± 0.03 for the NW, respectively. The ratio of Fe/O for NWs is underestimated because the oxygen deficiencies are compensated by foreign molecules (oxygen and water molecules) through adsorption due to large density of the unstable surface state of NWs [16]. The above EELS results demonstrate that the hard ball models can explain the formation the oxygen-vacancy ordering in different plane of α-Fe_2O_3 NWs.

4. Conclusions

In summary, we studied long-range ordering of oxygen-vacancy plane in α-Fe_2O_3 NWs. We found that there are two oxygen-vacancy-ordered superstructures from different planes in α-Fe_2O_3 NWs, which have an equivalent ordering distance. These two long-range-ordering superstructures were explained by introduction of oxygen vacancies in the planes of ten period distance of $(30\bar{3}0)$ and six period distance of $(11\bar{2}0)$ in the α-Fe_2O_3 NWs. Both oxygen-vacancy planes share similar ordering distances of 1.45 and 1.5 nm, and lie parallel to the growth direction of the NWs. Oxygen-vacancy orderings are created in α-Fe_2O_3 NWs due to the increased mobility of iron atoms and the unavailable oxygen atoms during the growth of α-Fe_2O_3 NWs at high temperature. Fe/O ratios are 0.7407 and 0.7273 for the two oxygen-vacancy orderings, respectively, very close to 0.7500 of the ratio of Fe_3O_4, which can explain the observed similar oxygen-vacancy ordering in different planes of α-Fe_2O_3 NWs.

Acknowledgements

We would like to thank the financial support from the National Key Basic Research Development Program of China (Grant No.: 2012CB722705), the National Natural Science Foundation of China (Grant No.: 10974105), the Natural Science Foundation for Outstanding Young Scientist in Shandong Province (Grant no.: JQ201002) and High-end Foreign Experts Recruitment Programs (Grant Nos.: GDW20173500154, GDW20163500110). Y. Q. Wang would also like to thank the financial support from the Top-notch Innovative Talent Program of Qingdao City (Grant No.: 13-CX-08), the Taishan Scholar Program of Shandong Province, Qingdao International Center for Semiconductor Photoelectric Nanomaterials, and Shandong Provincial University Key Laboratory of Optoelectrical Material Physics and Devices.

References

[1] W.J. Mai, L.H. Du, L.X. Shen, S.Z. Tan, Z.G. Zang, C.X. Zhao, Flexible electrochromic supercapacitor hybrid electrodes based on tungsten oxide films and silver nanowires, Chem. Comm. 52 (2016) 6296–6299.
[2] H.B. Wu, H.H. Hng, X.W. Lou, Direct synthesis of anatase TiO_2 nanowires with enhanced photocatalytic activity, Adv. Mater. 24 (2012) 2567–2571.
[3] T. Mushove, T.M. Breault, L.T. Thompson, Synthesis and characterization of hematite nanotube arrays for photocatalysis, Ind. Eng. Chem. Res. 54 (2015) 4285–4292.
[4] A. Kagar, J. Khamwannah, C.R. Liu, N. Park, D. Wang, S.A. Dayeh, S. Jin, Nanowire/nanotube array tandem cells for overall solar neutral water splitting, Nano Energy 19 (2016) 289–296.
[5] J. Chen, L. Xu, W. Li, X. Gou, α-Fe_2O_3 nanotubes in gas sensor and lithium-ion battery applications, Adv. Mater. 17 (2005) 582–586.
[6] N.M. Rashid, N. Kishi, T. Soga, Effects of nanostructures on iron oxide based dye sensitized solar cells fabricated on iron foils, Mater. Res. Bull. 77 (2016) 126–130.
[7] Y. Jiao, Y. Liu, B.S. Yin, S.W. Zhang, F.Y. Qu, X. Wu, Hybrid α-Fe_2O_3@NiO heterostructures for flexible and high performance supercapacitor electrodes and visible light driven photocatalysts, Nano Energy 10 (2014) 90–98.
[8] Y. Peng, H.L. Zhang, S.L. Pan, H.L. Li, Magnetic properties and magnetization reversal of α-Fe nanowires deposited in alumina film, J. Appl. Phys. 87 (2000) 7405–7408.
[9] D. Chen, L. Gao, A facile route for high-throughput formation of single-crystal α-Fe_2O_3 nanodisks in aqueous solutions of Tween 80 and triblock copolymer, Chem. Phys. Lett. 395 (2004) 316–320.
[10] L.S. Zhong, J.S. Hu, H.P. Liang, A.M. Cao, W.G. Song, L.J. Wan, Self-assembled 3D flowerlike iron oxide nanostructures and their application in water treatment, Adv. Mater. 18 (2006) 2426–2431.
[11] J. Jin, S. Ohkoshi, K. Hashimoto, Giant coercive field of nanometer-sized iron oxide, Adv. Mater. 16 (2004) 48–51.
[12] J.J. Wu, Y.L. Lee, H.H. Chiang, D.K. Wong, Growth and magnetic properties of oriented α-Fe_2O_3 nanorods, J. Phys. Chem. B 110 (2006) 18108–18111.

[13] Q. Han, Y.Y. Xu, Y.Y. Fu, H. Zhang, R.M. Wang, T.M. Wang, Z.Y. Chen, Defects and growing mechanisms of α-Fe_2O_3 nanowires, Chem. Phys. Lett. 431 (2006) 100–103.
[14] Y.L. Chueh, M.W. Lai, J.Q. Liang, L.J. Chou, Z.L. Wang, Systematic study of the growth of aligned arrays of α-Fe_2O_3 and Fe_3O_4 nanowires by a vapor-solid process, Adv. Funct. Mater. 16 (2006) 2243–2251.
[15] F. Liu, P.J. Cao, H.R. Zhang, J.F. Tian, C.W. Xiao, C.M. Shen, J.Q. Li, H.J. Gao, Novel nanopyramid arrays of magnetite, Adv. Mater. 17 (2005) 1893–1897.
[16] Y.C. Lee, Y.L. Chueh, C.H. Hsieh, M.T. Chang, L.J. Chou, Z.L. Wang, Y.W. Lan, C.D. Chen, H. Kurata, S. Isoda, p-type α-Fe_2O_3 nanowires and their n-type transition in a reductive ambient, Small 3 (2007) 1356–1361.
[17] M.T. Chang, L.J. Chou, C.H. Hsieh, Y.L. Chueh, Z.L. Wang, Y. Murakami, D. Shindo, Magnetic and electrical characterizations of half-metallic Fe_3O_4 nanowires, Adv. Mater. 19 (2007) 2290–2294.
[18] H.H. Zhu, J.X. Deng, J. Chen, R.B. Yu, X.R. Xing, Growth of hematite nanowire arrays during dense pentlandite oxidation, J. Mater. Chem. A 2 (2014) 3008–3014.
[19] Z.Q. Chen, U. Cvelbar, M. Mozetič, J.Q. He, M.K. Sunkara, Long-range ordering of oxygen-vacancy planes in α-Fe_2O_3 nanowires and nanobelts, Chem. Mater. 20 (2008) 3224–3228.
[20] U. Cvelbar, Z.Q. Chen, M.K. Sunkara, M. Mozetič, Spontaneous growth of super-structure α-Fe_2O_3 nanowires and nanobelt arrays in reactive oxygen plasma, Small 4 (2008) 1610–1614.
[21] L. Yuan, R.S. Cai, J.I. Jang, W.H. Zhu, C. Wang, Y.Q. Wang, G.W. Zhou, Morphological transformation of hematite nanostructures during oxidation of iron, Nanoscale 5 (2013) 7581–7588.
[22] R.S. Cai, T. Li, Y.Q. Wang, C. Wang, L. Yuan, G.W. Zhou, Formation of modulated structures in single-crystalline hexagonal α-Fe_2O_3 nanowires, J. Nanopart. Res. 14 (2012) 1–11.
[23] L. Yuan, Y.Q. Wang, R.S. Cai, Q.K. Jiang, J.B. Wang, B.Q. Li, A. Sharma, G.W. Zhou, The origin of hematite nanowire growth during the thermal oxidation of iron, Mater. Sci. Eng. B 177 (2012) 327–336.
[24] A.G. Nasibulin, S. Rackauskas, H. Jiang, Y. Tian, P.R. Mudimela, S.D. Shandakov, L.I. Nasibulina, J. Sainio, E.I. Kauppinen, Simple and rapid synthesis of α-Fe_2O_3 nanowires under ambient conditions, Nano Res. 2 (2009) 373–379.
[25] H. Srivastava, P. Tiwari, A.K. Srivastava, R.V. Nandedkar, Growth and characterization of α-Fe_2O_3 nanowires, J. Appl. Phys. 102 (2007) 054303.
[26] F. Qin, N.P. Magtoto, M. Garza, J.A. Kelber, Oxide film growth on Fe (111) and scanning tunneling microscopy induced high electric field stress in Fe_2O_3/Fe (111), Thin Solid Films 444 (2003) 179–188.
[27] C. Colliex, T. Manoubi, C. Ortiz, Electron-energy-loss-spectroscopy near-edge fine structures in the iron-oxygen system, Phys. Rev. B 44 (1991) 11402.
[28] D.H. Pearson, B. Fultz, C.C. Ahn, Measurements of 3d state occupancy in transition metals using electron energy loss spectrometry, Appl. Phys. Lett. 53 (1988) 1405–1407.